J. Phys.: Condens. Matter **11** (1999) 59–79. Printed in the UK PII: S0953-8984(99)94871-3

Low-frequency dynamics in an antiferromagnetic superlattice

N Papanicolaou

Department of Physics, University of Crete, and Research Centre of Crete, Heraklion, Greece

Received 8 June 1998, in final form 11 September 1998

Abstract. We present a theoretical study of the surface spin-flop transition which occurs in Fe/Cr multilayer films. The low-frequency response is effectively reduced to the dynamics of an antiferromagnetic discrete sine–Gordon equation due to the strong demagnetizing field created by out-of-plane fluctuations. We thus carry out a detailed calculation of dynamic susceptibilities which confirms and completes earlier theoretical work, and may suggest further experimental investigation of some of the more intricate aspects of this subject.

1. Introduction

Interesting effects that could, in principle, be observed near the free surface of a crystalline antiferromagnet were theoretically predicted some time ago [1–3]. The subject was recently revived and significantly expanded with the advent of multilayer magnetic films that may be thought of as synthetic superlattices [4]. Hence the early ideas were realized in the case of an Fe/Cr(211) superlattice grown on a MgO(110) substrate [5]. Under such conditions each Fe film acquires a twofold in-plane anisotropy, and the exchange coupling between neighbouring films is antiferromagnetic when the thickness of the Cr layer is equal to 11 Å. The typical thickness of each Fe layer lies in the range 20–40 Å and samples currently synthesized contain about 20 such layers.

An important element is the surface spin-flop (SSF) transition predicted and experimentally observed [6] to occur at a critical bias field which is smaller than the field required to induce the more familiar bulk spin-flop (BSF) transition roughly by a factor $\sqrt{2}$. However, the finer details of the SSF transition turned out to be rather intricate and lead to some apparently conflicting claims in the literature [7, 8]. The picture was substantially clarified in [9] and further discussed by the author [10] in relation to the ferromagnetic moment of an antiferromagnetic domain wall [11].

In a parallel development the dynamics of an Fe/Cr superlattice was studied using Brillouin scattering [12, 13] or response to a low-frequency AC magnetic field [14], the two cases being distinguished mainly by the different behaviour of the dipolar coupling in the respective frequency ranges. The current effort was directly inspired by [14] and intends to provide a simplified treatment valid at low frequencies, with due attention to the finer details of the SSF transition discussed in [10].

In section 2 the problem is reduced to the dynamics of what may be called an antiferromagnetic sine–Gordon equation. In section 3 we give a simple account of surface magnon modes and present some new exact results. We also make a first attempt to classify a host of critical or characteristic fields which are pertinent to a precise understanding of the phase transitions that take place on a finite superlattice. The SSF transition is further discussed

0953-8984/99/010059+21$19.50

in section 4 in preparation for a complete calculation of dynamic susceptibilities given in section 5. A few general comments are included in section 6 and an appendix provides some consistency checks in a simplified context.

2. Formulation

We consider an Fe/Cr superlattice whose consecutive Fe films are labelled by an index $\ell = 1, 2, \ldots, \Lambda$ where Λ is the total number of layers. Each Fe film carries a macroscopic magnetic moment $\boldsymbol{M}_\ell = (M_\ell^x, M_\ell^y, M_\ell^z)$ which is assumed to be coherent within each layer in the sense that it changes as a whole in response to interactions with neighbouring moments or with applied fields [14]. It is then natural to postulate that the dynamics is equivalent to that of a classical spin chain with Λ sites and is governed by the Landau–Lifshitz equation [15] in the form given by Gilbert [16] and further discussed by Kikuchi [17]:

$$\frac{\partial \boldsymbol{M}_\ell}{\partial t} + \gamma\left(\boldsymbol{M}_\ell \times \frac{\partial \boldsymbol{M}_\ell}{\partial t}\right) = \boldsymbol{M}_\ell \times \boldsymbol{F}_\ell \qquad \boldsymbol{F}_\ell = -\frac{\partial W}{\partial \boldsymbol{M}_\ell} \qquad \boldsymbol{M}_\ell^2 = 1 \tag{2.1}$$

where W is an energy functional and γ is a dissipation constant. This choice of dissipation appears to be suitable for the current problem because it preserves the magnitude of each moment. The latter has been normalized to unity and thus its physical unit is equal to the ferromagnetic moment of each Fe film. The dissipation constant γ is then dimensionless.

The energy functional consists of three terms corresponding to exchange, anisotropy, and Zeeman interactions, namely

$$W = \sum_{\ell=1}^{\Lambda-1} J(\boldsymbol{M}_\ell \cdot \boldsymbol{M}_{\ell+1}) + \frac{1}{2}\sum_{\ell=1}^{\Lambda}[K_1(M_\ell^x)^2 + K_2(M_\ell^y)^2 + K_3(M_\ell^z)^2] - \sum_{\ell=1}^{\Lambda}(\boldsymbol{H} \cdot \boldsymbol{M}_\ell) \tag{2.2}$$

where J is a positive exchange constant, K_1, K_2, and K_3 are anisotropy constants, and $\boldsymbol{H}$ is an applied field. As a consequence the effective field in equation (2.1) is given by

$$\boldsymbol{F}_\ell = -J(\boldsymbol{M}_{\ell+1} + \boldsymbol{M}_{\ell-1}) - (K_1 M_\ell^x \boldsymbol{e}_1 + K_2 M_\ell^y \boldsymbol{e}_2 + K_3 M_\ell^z \boldsymbol{e}_3) + \boldsymbol{H} \tag{2.3}$$

where $\boldsymbol{e}_1$, $\boldsymbol{e}_2$, and $\boldsymbol{e}_3$ are unit vectors along the three axes. One should keep in mind that the exchange term contains only one moment when it is applied for the outer layers ($\ell = 1$ or Λ).

All constants including the external field are measured in units of frequency thanks to the normalization $\boldsymbol{M}_\ell^2 = 1$ adopted in equation (2.1). It is also clear that the anisotropy constants may be restricted to

$$K_1 = 0 \qquad K_2 \equiv D \qquad K_3 \equiv D_0 \tag{2.4}$$

without loss of generality because all Ks can be shifted by a common constant without affecting the equation of motion. Furthermore, the xy-plane is taken to coincide with the plane of each layer, with the x-axis pointing along the easy axis, while the z-axis points along the chain direction. Accordingly the positive constant D is the strength of the in-plane easy-axis anisotropy, and the positive constant D_0 provides an effective description of the intrafilm demagnetizing field. The interfilm dipolar coupling [18] may be neglected at low wavenumbers of current interest [12, 14]. For the moment we also assume that the external field is uniform and is applied along the easy axis:

$$\boldsymbol{H} = (H, 0, 0) = H\boldsymbol{e}_1. \tag{2.5}$$

Typical values of the parameters given in [14] are $D_0/J \sim 21$ and $D/J \sim 1/4$, while the most interesting effects are observed for modest bias fields in the kG range which corresponds to $H/J \sim 1$. Therefore we are in a situation where the strong inequalities

$$D_0 \gg D, J, H \tag{2.6}$$

are reasonably well satisfied and imply that out-of-plane fluctuations are significantly suppressed.

The appearance of a disparate scale (D_0) makes the Landau–Lifshitz equation awkward but can be turned to advantage by a truncation of the dynamics capitalizing on the fact that out-of-plane fluctuations may be treated as small perturbations. The idea of truncation was first implemented by Mikeska for a planar ferromagnetic chain [19] and is also implicit in his subsequent treatment of antiferromagnetic chains [20]. A more complete account of the latter problem was given in [21, 22]. The present author first tested the domain of validity of the truncated dynamics in a simple model containing only one moment. The results strongly influenced his decision to adopt such an approach in the current problem and are thus briefly described in the appendix.

The steps of the derivation are elementary and proceed by introducing the familiar spherical parametrization

$$M_\ell^x = \sin\theta_\ell \cos\phi_\ell \qquad M_\ell^y = \sin\theta_\ell \sin\phi_\ell \qquad M_\ell^z = \cos\theta_\ell \tag{2.7}$$

in equation (2.2) to produce an energy functional $W = W(\theta, \phi)$. The general form of the Landau–Lifshitz equation (2.1) then reads

$$\sin\theta_\ell \frac{\partial\phi_\ell}{\partial t} + \gamma \frac{\partial\theta_\ell}{\partial t} = -\frac{\partial W}{\partial\theta_\ell} \qquad \sin\theta_\ell \frac{\partial\theta_\ell}{\partial t} - \gamma \sin^2\theta_\ell \frac{\partial\phi_\ell}{\partial t} = \frac{\partial W}{\partial\phi_\ell}. \tag{2.8}$$

At vanishing dissipation ($\gamma = 0$) the preceding equations are in the standard Hamiltonian form; we note that the variable $\pi_\ell = \cos\theta_\ell$ is canonically conjugate to the azimuthal angle ϕ_ℓ.

In order to derive the truncated dynamics it is convenient to consider the rescaled variables

$$\rho = \sqrt{J/D_0} \qquad \Omega_0 = \sqrt{J D_0} \qquad \tau = \Omega_0 t \tag{2.9}$$

where the dimensionless ratio $\rho \ll 1$ controls the size of out-of-plane fluctuations, Ω_0 sets a unit for frequency, and τ is a dimensionless time variable. One could use a different scale, say, D instead of J in equation (2.9) but this is only a matter of convenience as long as the inequalities (2.6) are all satisfied (see the appendix). The list of rationalized parameters is completed with

$$\delta = D/J \qquad \mathfrak{h} = H/J \qquad \lambda = \gamma/\rho \tag{2.10}$$

for the in-plane easy-axis anisotropy, the applied field, and the dissipation constant, respectively. Implicit in the last relation is the assumption $\gamma \ll 1$ which is certainly reasonable and must supplement the inequalities (2.6). Finally we make the change of variables

$$\theta_\ell = \frac{\pi}{2} - \rho\chi_\ell \tag{2.11}$$

anticipating the fact that the component of the magnetic moment along the chain direction is small when $\rho \ll 1$.

Inserting the above variables in (2.8) leads to a system of coupled equations which appear to be rather complicated. However, substantial simplifications occur in the limit of small ρ. The final result is simple and self-explanatory and is thus stated here without further ado:

$$\chi_\ell = \dot\phi_\ell \qquad \ddot\phi_\ell + \lambda\dot\phi_\ell = f_\ell \tag{2.12}$$

where the dot denotes differentiation with respect to τ and the 'force' f_ℓ is derived from the 'potential'

$$V = \sum_{\ell=1}^{\Lambda-1} \cos(\phi_\ell - \phi_{\ell+1}) + \sum_{\ell=1}^{\Lambda} \left(\frac{\delta}{2} \sin^2\phi_\ell - \mathfrak{h}\cos\phi_\ell \right) \tag{2.13}$$

according to the standard prescription:

$$f_\ell = -\frac{\partial V}{\partial \phi_\ell} = \sin(\phi_\ell - \phi_{\ell+1}) + \sin(\phi_\ell - \phi_{\ell-1}) - \delta \cos\phi_\ell \sin\phi_\ell - \mathfrak{h} \sin\phi_\ell. \tag{2.14}$$

Again only one of the (exchange) sine terms is present at the outer layers. The second relation in (2.12) is an antiferromagnetic discrete sine–Gordon equation including dissipation and the first relation provides a lowest-order approximation of θ_ℓ in equation (2.11). Substituting this in equation (2.7) yields

$$M_\ell^x \approx \left(1 - \frac{1}{2}\rho^2 \dot\phi_\ell^2\right) \cos\phi_\ell \qquad M_\ell^y \approx \left(1 - \frac{1}{2}\rho^2 \dot\phi_\ell^2\right) \sin\phi_\ell \qquad M_\ell^z \approx \rho \dot\phi_\ell. \tag{2.15}$$

Therefore, given a solution $\phi_\ell = \phi_\ell(\tau)$ of the discrete sine–Gordon equation, the original magnetic moments are completely specified to leading order in ρ. The sine–Gordon equation contains only the rationalized parameters (2.10) and will provide the basis for all subsequent calculations.

This section is concluded with a few general comments. We think that the conventions and notation used here are well suited for the present work but differ significantly from those of most previous studies including our own [10, 11]. In particular, the field $\mathfrak{h}$ of equation (2.10) differs from the field h of the above references by the rescaling $\mathfrak{h} = 2\varepsilon h$, where ε is related to the easy-axis anisotropy as $\delta = \varepsilon^2$. Such a rescaling is very convenient in the discussion of the continuum limit of bulk domain walls, which play an important role in this subject, but would lead to unnecessary notational complications in the current work. Therefore, to avoid any confusion, the continuum limit will not be discussed in the present paper. Furthermore, numerical calculations will be carried out for the specific anisotropy $\delta = 1/4$ or $\varepsilon = 1/2$ for which the two definitions of the rationalized field become identical.

3. Surface magnon modes

The central mathematical problem consists of finding the minimum (ground state) of the effective potential V. It should be stressed that the minimum of this reduced potential coincides with that of the original energy functional W irrespective of the specific value of D_0. In other words, the truncation of the dynamics at large D_0 discussed in section 2 does not affect the ground state itself, even though it certainly simplifies the dynamics of fluctuations.

The nature of the ground state is highly nontrivial on a finite chain and depends crucially on the strength of the bias field $\mathfrak{h}$. Yet one should expect that the simple Néel state $\phi_\ell = \phi_\ell^{(0)} = (0, \pi, 0, \pi, \ldots)$ is the minimum-energy configuration for a sufficiently weak bias field. Our immediate task is then to examine the domain of local stability of the Néel state for various values of $\mathfrak{h}$. Hence we return to the second equation in (2.12), applied for vanishing dissipation ($\lambda = 0$), and linearize it by setting $\phi_\ell = \phi_\ell^{(0)} + \psi_\ell$ and neglecting nonlinear terms in ψ_ℓ to obtain

$$\begin{aligned} &\ddot\psi_1 + (\psi_1 - \psi_2) + (\delta + \mathfrak{h})\psi_1 = 0 \\ &\ddot\psi_\ell + (2\psi_\ell - \psi_{\ell+1} - \psi_{\ell-1}) + [\delta - (-1)^\ell \mathfrak{h}]\psi_\ell = 0 \qquad \ell = 2, 3, \ldots, \Lambda - 1 \\ &\ddot\psi_\Lambda + (\psi_\Lambda - \psi_{\Lambda-1}) + (\delta - \mathfrak{h})\psi_\Lambda = 0. \end{aligned} \tag{3.1}$$

Here we assume that the total number of layers is even ($\Lambda = 2N$). The case of an odd superlattice ($\Lambda = 2N + 1$) will not be discussed until section 6.

The normal modes of the linearized system (3.1) are calculated by first making the replacement $\ddot\psi_\ell \to -\omega^2 \psi_\ell$ where ω is a characteristic frequency. We also introduce sublattice

variables according to $\alpha_n = \psi_{2n-1}$ and $\beta_n = \psi_{2n}$, with $n = 1, 2, \ldots, N$, to write

$$\begin{aligned}
&(\eta - 1 + \mathfrak{h})\alpha_1 = \beta_1 \\
&(\eta + \mathfrak{h})\alpha_n = \beta_{n-1} + \beta_n \qquad n = 2, 3, \ldots, N \\
&(\eta - \mathfrak{h})\beta_n = \alpha_n + \alpha_{n+1} \qquad n = 1, 2, \ldots, N-1 \\
&(\eta - 1 - \mathfrak{h})\beta_N = \alpha_N
\end{aligned} \tag{3.2}$$

where $\eta = 2 + \delta - \omega^2$ is used as a temporary notational abbreviation.

Analytical solution of this linear system is complicated by the appearance of the two distinct equations at the outer layers. Thus it is useful to consider for the moment the case of a cyclic chain where the first and fourth equations in (3.2) are absent and the remaining ones may be written as

$$\beta_n = \frac{\alpha_n + \alpha_{n+1}}{\eta - \mathfrak{h}} \qquad (\eta^2 - \mathfrak{h}^2)\alpha_n = 2\alpha_n + \alpha_{n+1} + \alpha_{n-1} \tag{3.3}$$

and are valid for all n. An explicit solution is now given by $\alpha_n = \mathrm{e}^{\mathrm{i}qn}$ where $q = 2\pi\nu/N$, with $\nu = 0, 1, \ldots, N-1$, is a sublattice momentum, provided that

$$\eta^2 = 4\cos^2(q/2) + \mathfrak{h}^2.$$

This eigenvalue condition leads to two branches of normal frequencies:

$$\omega_\pm^2(q) = 2 + \delta \pm \sqrt{4\cos^2(q/2) + \mathfrak{h}^2} \tag{3.4}$$

which may be referred to as the 'optical' and 'acoustical' branches. The frequencies (3.4) are measured in units of the fundamental frequency Ω_0 of equation (2.9) and are valid for large D_0, as explained in section 2.

The normal frequencies of a cyclic chain are contained within the two shaded regions of figure 1 which are bounded by the four lines $\omega_\pm(q = 0)$ and $\omega_\pm(q = \pi)$ viewed as functions of the applied field. For each field value there exist N eigenvalues in each branch and their distribution becomes dense as $N \to \infty$. It is evident that the acoustical branch is

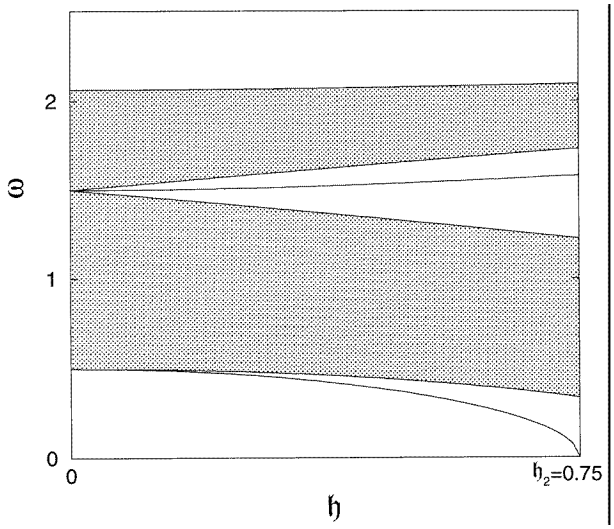

Figure 1. Schematic illustration of the magnon spectrum in the Néel state as a function of the bias field. The two distinct gap modes are given analytically by equations (3.5) and (3.6). Here and in all subsequent illustrations we use the specific anisotropy $\delta = 1/4$.

itself separated from the ground state by a gap and a similar gap opens between the acoustical and optical branches at any finite field. This picture remains substantially correct on an open chain with some important deviations. The eigenvalues are somewhat rearranged within each continuum while each branch loses exactly one eigenvalue that becomes a gap mode. Therefore there exist two distinct gap modes.

Although we have been unable to derive an analytical solution for the complete spectrum of an open chain the two gap modes can be calculated explicitly. Indeed one may return to the linear system (3.2) and verify all four equations by direct substitution of the following two special solutions:

$$\omega^2 = \omega_1^2 = 1 + \delta - \sqrt{1 + \mathfrak{h}^2} \qquad \alpha_n = \xi^{N-n+1} \qquad \beta_n = \xi^{N-n} \tag{3.5}$$

and

$$\omega^2 = \omega_2^2 = 1 + \delta + \sqrt{1 + \mathfrak{h}^2} \qquad \alpha_n = (-1)^{n-1}\xi^{n-1} \qquad \beta_n = (-1)^n \xi^n \tag{3.6}$$

where, in both cases,

$$\xi = \sqrt{1 + \mathfrak{h}^2} - \mathfrak{h} \qquad 0 < \xi < 1 \tag{3.7}$$

and $n = 1, 2, \ldots, N$. The mode (3.5) is exponentially localized near the rightmost layer, where the applied field opposes the Néel moment, and its frequency ω_1 lies within the lowest gap in figure 1. Similarly the mode (3.6) is localized near the leftmost layer, where the field is parallel to the Néel moment, and its frequency ω_2 lies within the middle gap.

The significance of these surface magnon modes is that the lowest one becomes soft ($\omega_1 = 0$) at a critical field

$$\mathfrak{h}_2 = \sqrt{2\delta + \delta^2} \tag{3.8}$$

beyond which the Néel state ceases to be stable even locally, as discussed by Mills and Saslow for a semi-infinite system [2]. The present derivation together with the remarks included in the first paragraph of this section establish that the critical field (3.8) is actually exact on an open even chain of any size. The fate of the ground state for $\mathfrak{h} > \mathfrak{h}_2$ is a nontrivial question that cannot be addressed within the linearized theory. One should also note that the Néel state could, in principle, become globally unstable at an earlier stage ($\mathfrak{h} < \mathfrak{h}_2$) through a first-order transition. These important issues will be taken up in section 4 by a direct numerical minimization of the effective potential V.

Nevertheless, some further general features of the anticipated results can be surmised from an elementary analysis of a *cyclic* chain for which the ground state can be analytically constructed for all $\mathfrak{h}$. Surface modes are, of course, absent in this case and the system would proceed directly to the familiar BSF transition at a critical field that is higher than $\mathfrak{h}_2$. In fact, the BSF transition is first order and is characterized by three critical fields [11]

$$\mathfrak{h}_{3a} = (4 - \delta)\sqrt{\frac{\delta}{4 + \delta}} \qquad \mathfrak{h}_{3b} = \sqrt{4\delta - \delta^2} \qquad \mathfrak{h}_{3c} = \sqrt{4\delta + \delta^2} \tag{3.9}$$

ordered as $\mathfrak{h}_{3a} < \mathfrak{h}_{3b} < \mathfrak{h}_{3c}$. The Néel state is locally stable for $\mathfrak{h} < \mathfrak{h}_{3c}$ as is evident from the bulk magnon spectrum (3.4) whose lowest eigenvalue $\omega_-(q = 0)$ vanishes at $\mathfrak{h} = \mathfrak{h}_{3c}$. Actually the Néel state is rendered globally unstable at an earlier stage to become a canted state $\phi_\ell = (-1)^\ell \phi_0$ with

$$\cos\phi_0 = \frac{\mathfrak{h}}{4 - \delta}. \tag{3.10}$$

The canted state is locally stable for $\mathfrak{h} > \mathfrak{h}_{3a}$ but has higher energy than the Néel state until the field reaches the value $\mathfrak{h}_{3b}$ after which the role of the two states is interchanged. Therefore,

strictly speaking, the BSF transition occurs at the critical field $\mathfrak{h}_{3b}$. However, all three fields in equation (3.9) are important in connection with hysteresis that would be observed near the first-order BSF transition on a cyclic chain. The three fields become indistinguishable in the limit of weak easy-axis anisotropy, namely $\mathfrak{h}_{3a} \approx \mathfrak{h}_{3b} \approx \mathfrak{h}_{3c} \approx \sqrt{4\delta}$, and differ from the field $\mathfrak{h}_2 \approx \sqrt{2\delta}$ in the same limit by the well-known factor $\sqrt{2}$.

The magnon spectrum in the canted state of a cyclic chain is similarly derived to yield

$$\omega_{\pm}^2(q) = 2[c_1 \pm c_2 \cos(q/2)] \qquad c_1 = 1 - \frac{\delta}{2}\sin^2\phi_0 \qquad c_2 = 2\sin^2\phi_0 - 1 \tag{3.11}$$

and its lowest squared eigenvalue $\omega_-^2(q = 0) = 2(c_1 - c_2)$ is non-negative for $\mathfrak{h} \geqslant \mathfrak{h}_{3a}$, in accord with our interpretation of the critical fields (3.9). The spectrum shows an interesting behaviour when the field is increased beyond the BSF transition. Hence the coefficient c_2 vanishes at the characteristic field

$$\mathfrak{h}_{ch} = (4 - \delta)/\sqrt{2} \qquad c_2 = 0 \tag{3.12}$$

where the dispersion collapses to the single value $\omega_{\pm}^2 = 2c_1 = (4 - \delta)/2$ for all q. Above $\mathfrak{h}_{ch}$ the lowest boundary of the spectrum is given by $\omega_+^2(q = 0) = 2(c_1 + c_2)$ and vanishes at yet another critical field

$$\mathfrak{h}_4 = 4 - \delta \tag{3.13}$$

beyond which the systems orders ferromagnetically ($\phi_\ell = 0$). The magnon spectrum for $\mathfrak{h} > \mathfrak{h}_4$ reads

$$\omega^2(k) = \delta + \mathfrak{h} - 2(1 - \cos k) \tag{3.14}$$

where $k = 2\pi\lambda/\Lambda$, with $\lambda = 0, 1, \ldots, \Lambda - 1$, is now the crystal momentum on the complete lattice. The lowest eigenvalue occurs at the zone boundary ($k = \pi$) and becomes soft at $\mathfrak{h} = \mathfrak{h}_4$.

Needless to say, some departures from the preceding picture should be expected to occur on an open chain. In particular, interesting surface magnon modes occur also for $\mathfrak{h} > \mathfrak{h}_2$ but an analytical treatment seems impossible. Therefore we turn to numerical calculation of the magnon spectrum for all $\mathfrak{h}$, in section 5, after the true ground state has been determined in section 4.

4. Surface spin-flop transition

This section is a simplified version of [10]. We consider a numerical minimization of the effective potential V for a wide range of field values. An elementary algorithm may be based on the dissipative sine–Gordon equation (2.12). A further simplification is possible if one only desires to compute the minima of the potential. One may then employ the fully dissipative equation

$$\dot{\phi}_\ell = f_\ell = -\frac{\partial V}{\partial \phi_\ell} \tag{4.1}$$

in the sense that an arbitrarily chosen initial configuration ϕ_ℓ will eventually relax to a terminal state $\phi_\ell^{(0)}$ that is a local minimum of the potential. The resulting equilibrium spin configuration is given by

$$M_\ell^x = \cos\phi_\ell^{(0)} \equiv Q_\ell^x \qquad M_\ell^y = \sin\phi_\ell^{(0)} \equiv Q_\ell^y \qquad M_\ell^z = 0 \tag{4.2}$$

which is a static version of equation (2.15).

A straightforward first-order time differencing (Euler) scheme, with a time step in the neighbourhood of 10^{-2}, proved to be sufficient for an accurate determination of the terminal

states of equation (4.1). Numerical calculations were performed on an even chain with $\Lambda = 20$ sites and a specific easy-axis anisotropy $\delta = 1/4$ which are typical values in currently synthesized superlattices [14]. The picture would be significantly different for very large anisotropy [9], as is also evident in the discussion of section 3 from the repeated appearance of the quantity $4 - \delta$ which becomes negative for $\delta > 4$.

The Néel state $\phi_\ell = (0, \pi, \ldots, 0, \pi)$ is an exact static solution for any bias field but is locally stable only for $\mathfrak{h} < \mathfrak{h}_2 = 0.75$; the latter field value was obtained from equation (3.8) applied with $\delta = 1/4$. To verify this statement we consider a 'small' fluctuation in the Néel state realized here by replacing the last entry $\phi_\Lambda = \pi$ with, say, $\phi_\Lambda = 0.99\pi$. The resulting configuration is then used as initial condition in equation (4.1) which is solved by the elementary numerical algorithm described above. Not surprisingly the perturbed configuration quickly relaxes back to the Néel state as long as $\mathfrak{h} < \mathfrak{h}_2$. However, at $\mathfrak{h} = \mathfrak{h}_2$, the calculated terminal state is highly nontrivial and describes a domain wall that has suddenly nucleated somewhere between the rightmost layer and the centre of the superlattice; see figure 1 of [10].

The process is continued beyond $\mathfrak{h}_2$, now in steps of $\delta\mathfrak{h} = 10^{-3}$, using as initial configuration at each step the terminal state obtained in the preceding step. The domain wall quickly moves to the centre of the lattice and becomes symmetric about the centre to 16-place accuracy for $\mathfrak{h} \gtrsim 1$. This is roughly the field region of the would-be BSF transition predicted by the critical fields $\mathfrak{h}_3$ of equation (3.9). However, the BSF transition is rapid but not sharp on an open chain. Meanwhile the domain wall expands symmetrically with increasing field to become a nearly uniform canted state within the bulk with notable nonuniformities near the edges. Complete ferromagnetic order is eventually achieved when the field exceeds the value $\mathfrak{h} = 3.73$ which is slightly different from the critical field $\mathfrak{h}_4 = 4 - \delta = 3.75$ thanks to a minor finite-size effect. In this respect, one should recall that no such effect was observed for the critical field $\mathfrak{h}_2 = 0.75$ because equation (3.8) is exact on an open even chain of any size.

A good illustration is provided by the calculated total magnetic moment

$$\begin{aligned} \boldsymbol{\mu} &= \sum_{\ell=1}^{\Lambda} \boldsymbol{M}_\ell = (\mu_1, \mu_2, \mu_3) \\ \mu_1 &= \sum_{\ell} Q_\ell^x \qquad \mu_2 = \sum_{\ell} Q_\ell^y \qquad \mu_3 = 0 \end{aligned} \tag{4.3}$$

whose field dependence is shown by a solid line in figure 2. This figure uses a limited field range ($0 < \mathfrak{h} < 1.5$) to emphasize important details that are present in the spin-flop regime. The component μ_1 along the easy axis suffers a sudden jump at $\mathfrak{h}_2$ and also develops a shoulder near $\mathfrak{h} \sim \mathfrak{h}_3 \sim 1$ which reflects a rapid crossover at the BSF regime. Further increase of the applied field beyond the figure range leads to a monotonic increase of μ_1 until it reaches ferromagnetic saturation ($\mu_1 = \Lambda = 20$) at the critical field $\mathfrak{h}_4$. Finally, the inset of figure 2 demonstrates that a small transverse component μ_2 appears, just above $\mathfrak{h}_2$, which reflects the fact that the nucleated domain wall is initially off centre. The transverse moment μ_2 and the corresponding asymmetry of the domain wall about the centre disappear to 16-place accuracy for $\mathfrak{h} \gtrsim 1$.

The familiar BSF transition is thus pre-empted by a SSF transition. The latter will generically occur at the critical field $\mathfrak{h}_2$, where a surface magnon mode turns soft, if the ascending-field sequence is implemented without special precautions; e.g., by slowly increasing the applied field either in small steps or continuously. On the other hand, the sudden nucleation of a domain wall within the chain, the sudden jump of the total moment, and a corresponding sudden reduction of the energy, make it clear that the SSF transition is first order and could occur at a field smaller than $\mathfrak{h}_2$.

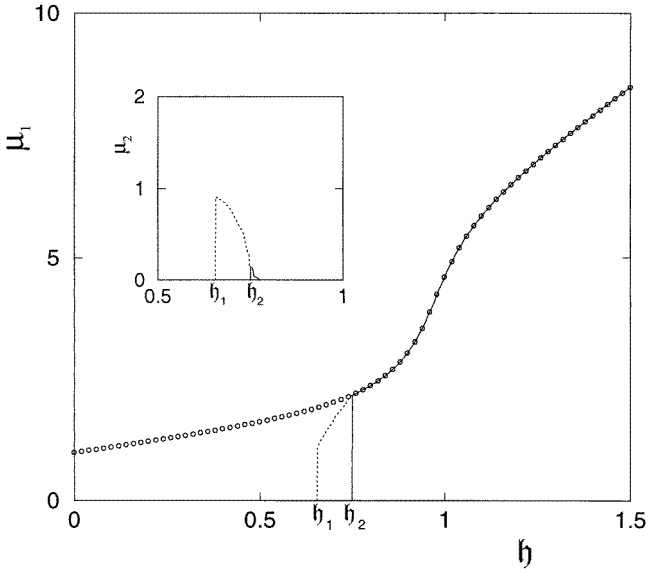

Figure 2. Total magnetic moment $\boldsymbol{\mu} = (\mu_1, \mu_2, \mu_3 = 0)$ for an open chain with $\Lambda = 20$ sites for the various field sequences as described in the text.

In order to probe for such a possibility we repeat the procedure by invoking a 'large' fluctuation in the initial Néel state. The moment of the outer layer is now nearly flipped by replacing its Néel value $\phi_\Lambda = \pi$ with, say, $\phi_\Lambda = 0.01\pi$. If we then use such an initial condition in equation (4.1) the perturbed configuration no longer relaxes to the pure Néel state when the field exceeds a new critical value $\mathfrak{h}_1 = 0.656$ which is smaller than $\mathfrak{h}_2 = 0.75$. Above $\mathfrak{h}_1$ the relaxed configuration is a nontrivial surface state in which the outer moment forms a nearly 60° angle to the easy axis and should thus be identified with the 'true' SSF state of [9]. We have continued the process beyond $\mathfrak{h}_1$, again in steps of $\delta\mathfrak{h} = 10^{-3}$, to find that the SSF state eventually evolves into the domain wall discussed earlier. Similarly the corresponding total magnetic moment, depicted by a dotted line in figure 2, joins *smoothly* with the earlier results at $\mathfrak{h}_2$. The appearance of a sizable transverse component μ_2 in the region $[\mathfrak{h}_1, \mathfrak{h}_2]$ implies that the SSF state is significantly twisted and comes in two varieties distinguished by their handedness. The transverse moment would be negative if the initial configuration were chosen such that $\phi_\Lambda = -0.01\pi$.

The calculated total moment displays a rather bumpy field dependence within the SSF region, which is not clearly visible on the scale of figure 2. To make this feature completely apparent we consider the static susceptibility

$$\chi_{11} = \frac{1}{\Lambda}\frac{\partial \mu_1}{\partial \mathfrak{h}} \tag{4.4}$$

which is plotted in figure 3 using both a dotted and a solid line corresponding to the two field sequences. The rounded maximum in the vicinity of $\mathfrak{h} \sim 1$ is due to the rapid crossover that has replaced a sharp BSF transition. The situation is far more complex in $[\mathfrak{h}_1, \mathfrak{h}_2]$ and even finer structure may emerge if the field step is chosen to be smaller than the currently employed $\delta\mathfrak{h} = 10^{-3}$. Therefore the details of figure 3 indicate a 'chaotic' behaviour in the otherwise 'deterministic' effective potential V defined on an open chain [7, 8]. Finally, the notation of equation (4.4) suggests that the susceptibility tensor also acquires nonvanishing off-diagonal

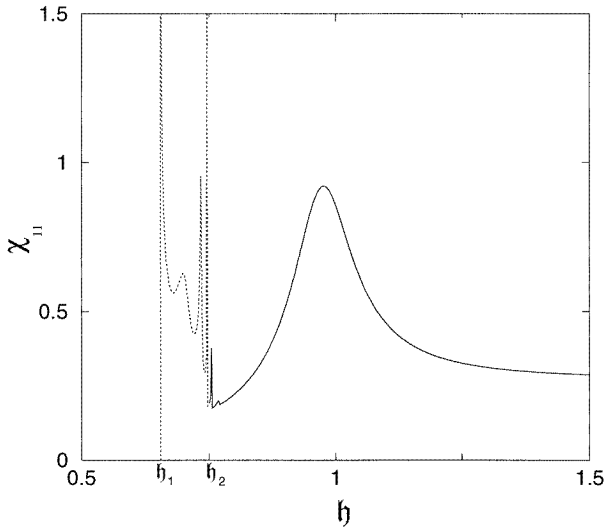

Figure 3. The static susceptibility of equation (4.4) using as input numerical data from figure 2.

elements due to the twisting effect described in the preceding paragraph. Such elements may be computed using our numerical results for the transverse moment μ_2 but this issue will not be pursued further.

We thus return to the main argument and examine whether or not a transition can actually occur at the critical field $\mathfrak{h}_1$. A contrived scenario for instigating such a transition is suggested by the method of calculation; namely, by temporarily applying a strong field pulse opposing the Néel moment at the outer layer as the bias field crosses the value $\mathfrak{h}_1$. A more natural alternative results from an appreciation of the detailed nature of the SSF transition. A closer examination of the numerical energy data reveals that we are dealing with a genuine first-order transition characterized by three distinct field values ordered as $\mathfrak{h}_1 < \mathfrak{h}_c < \mathfrak{h}_2$ where $\mathfrak{h}_1 = 0.656$ and $\mathfrak{h}_2 = 0.75$ are the fields already discussed. The low-energy data may be roughly interpreted by invoking an uneven double well whose two local minima correspond to the Néel and SSF states. The Néel state is locally stable for $\mathfrak{h} < \mathfrak{h}_2$ and the SSF state for $\mathfrak{h} > \mathfrak{h}_1$. The energies of the two minima coincide at the critical field $\mathfrak{h}_c = 0.682$ which lies in the overlapping domain $[\mathfrak{h}_1, \mathfrak{h}_2]$. The SSF state first appears as a metastable local minimum in $[\mathfrak{h}_1, \mathfrak{h}_c]$ and becomes the absolute minimum for $\mathfrak{h} > \mathfrak{h}_c$. Similarly the Néel state is the absolute minimum for $\mathfrak{h} < \mathfrak{h}_c$ and survives as a metastable local minimum in $[\mathfrak{h}_c, \mathfrak{h}_2]$. Beyond $\mathfrak{h}_2$ the SSF state has clearly transformed into a domain wall which is detached from the surface and quickly moves to the centre of the superlattice; in general agreement with the interpretation of [9] where the critical field $\mathfrak{h}_2$ is derived by a different reasoning and is thought to provide the phase boundary of the AF_3:AF_4 transition. We think that the coincidence of such a phase boundary with the boundary of local stability of the Néel state, i.e., the field where a surface magnon mode turns soft, is a model-dependent accident that is partly responsible for the confusion generated on this subject.

To summarize, the 'true' SSF transition occurs at the critical field $\mathfrak{h}_c$. Nevertheless, all three fields $\mathfrak{h}_1$, $\mathfrak{h}_c$, and $\mathfrak{h}_2$ are relevant in connection with hysteresis, $\mathfrak{h}_c$ being the least important. Specifically, let us invoke the original scenario and drive the system to a nominal field $\mathfrak{h}_0$, just above $\mathfrak{h}_2$, where a domain wall appears within the chain but is still off centre. If we then reverse the cycle by reducing the field adiabatically, the domain wall returns to the outer layer

through formation of the SSF state in reverse order, and finally exits the system at $\mathfrak{h} = \mathfrak{h}_1$ where the chain returns to the pure Néel state. Accordingly the total moment follows the solid line in figure 2 during the ascending-field sequence but the dotted line during the descending sequence, a fact that can be checked numerically provided that the nominal field $\mathfrak{h}_0$ is close to $\mathfrak{h}_2$. Therefore the 'true hysteresis loop' is given by the solid and dotted lines of figure 2 taken in combination.

It would thus appear that we have obtained a complete description of the SSF transition including hysteresis. Nonetheless, a further interesting possibility arises when the nominal field $\mathfrak{h}_0$ is chosen to be sufficiently large, practically in the region $\mathfrak{h}_0 > 0.8$, where the relaxed configuration is symmetric about the centre to great numerical precision which reaches machine (16-place) accuracy for $\mathfrak{h}_0 \gtrsim 1$. The calculated hysteresis curve is then rather elongated and typically extends all the way down to vanishing field [10, 12, 14], as shown in figure 2 by open circles starting from $\mathfrak{h}_0 = 1.5$. The explanation for a elongated hysteresis is that the domain wall loses its memory as the field descends through the SSF regime and remains trapped in a metastable state near the centre of the superlattice even at low field values. This possibility was previously discussed [10] as a means for experimental detection of the theoretically predicted ferromagnetic moment of an antiferromagnetic domain wall [11].

We conclude this section with a comment concerning the elementary Euler scheme used to solve the fully dissipative equation (4.1). One needs about 10^6–10^7 time steps of $\delta\tau = 10^{-2}$ to obtain complete relaxation for each field value within the SSF regime, a process that amounts to about one CPU minute on a modest workstation. The required number of time steps can be reduced by several orders of magnitude away from the critical region, and hence the whole numerical effort is well within current capabilities. Furthermore, the calculation was subjected to several consistency checks, including a fourth-order Runge–Kutta solution of the complete sine–Gordon equation (2.12) at finite λ.

5. Dynamic response

We now consider the response of the superlattice to an AC magnetic field applied in a direction that is perpendicular to both the easy axis and the chain direction. Such a field is accounted for by the simple substitution

$$\boldsymbol{F}_\ell \to \boldsymbol{F}_\ell + H_\perp \cos(\Omega t)\boldsymbol{e}_2 \tag{5.1}$$

in the original Landau–Lifshitz equation (2.1). Within the context of the truncated dynamics, the sine–Gordon equation (2.12) is accordingly extended to

$$\ddot{\phi}_\ell + \lambda\dot{\phi}_\ell = f_\ell + \mathfrak{h}_\perp \cos(\omega\tau)\cos\phi_\ell \tag{5.2}$$

where τ is given by equation (2.9), $\omega = \Omega/\Omega_0$ is the frequency in units of Ω_0, and $\mathfrak{h}_\perp = H_\perp/J$ is the amplitude of the AC field normalized as in equation (2.10).

With small variations of the main theme to be discussed later, the mathematical problem consists of the following simple steps. Suppose that the superlattice has relaxed in its ground-state configuration $\phi_\ell^{(0)}$ at a specific value of the bias field $\mathfrak{h}$. One must then solve equation (5.2) with initial condition

$$\phi_\ell(\tau = 0) = \phi_\ell^{(0)}$$

to determine the configuration $\phi_\ell(\tau)$ at all later times. Of special importance is the case of a weak transverse field which probes the intrinsic properties of the superlattice and allows us to invoke the linear approximation

$$\phi_\ell(\tau) \approx \phi_\ell^{(0)} + \mathfrak{h}_\perp u_\ell(\tau). \tag{5.3}$$

To lowest order in $\mathfrak{h}_\perp$, equation (5.2) becomes

$$\ddot{u}_\ell + \lambda\dot{u}_\ell + \sum_{m=1}^{\Lambda} C_{\ell m} u_m = Q_\ell^x \cos(\omega\tau) \tag{5.4}$$

where the nonvanishing elements of the tridiagonal $\Lambda \times \Lambda$ matrix $C = (C_{\ell m})$ are given by

$$\begin{aligned} C_{11} &= -(\boldsymbol{Q}_1 \cdot \boldsymbol{Q}_2) + \delta[(Q_1^x)^2 - (Q_1^y)^2] + \mathfrak{h} Q_1^x \\ C_{\ell\ell} &= -\boldsymbol{Q}_\ell \cdot (\boldsymbol{Q}_{\ell+1} + \boldsymbol{Q}_{\ell-1}) + \delta[(Q_\ell^x)^2 - (Q_\ell^y)^2] + \mathfrak{h} Q_\ell^x \\ C_{\Lambda\Lambda} &= -(\boldsymbol{Q}_\Lambda \cdot \boldsymbol{Q}_{\Lambda-1}) + \delta[(Q_\Lambda^x)^2 - (Q_\Lambda^y)^2] + \mathfrak{h} Q_\Lambda^x \\ C_{\ell,\ell+1} &= (\boldsymbol{Q}_\ell \cdot \boldsymbol{Q}_{\ell+1}) = C_{\ell+1,\ell} \end{aligned} \tag{5.5}$$

and are expressed entirely in terms of the two-component vector $\boldsymbol{Q}_\ell = (Q_\ell^x, Q_\ell^y)$ defined in equation (4.2) for a specific ground-state configuration $\phi_\ell^{(0)}$ calculated in section 4.

Thanks to dissipation, transients die out quickly and the terminal state is described by the particular solution of equation (5.4)

$$u_\ell(\tau) = A_\ell \cos(\omega\tau) + B_\ell \sin(\omega\tau) \tag{5.6}$$

where the local dynamic susceptibilities A_ℓ and B_ℓ satisfy the linear system of algebraic equations

$$\lambda\omega A_\ell = \sum_m D_{\ell m} B_m \qquad \lambda\omega B_\ell + \sum_m D_{\ell m} A_m = Q_\ell^x \qquad D \equiv C - \omega^2 I. \tag{5.7}$$

The matrix $D = (D_{\ell m})$ can readily be constructed in terms of the matrix C of equation (5.5) and the $\Lambda \times \Lambda$ unit matrix $I = \mathrm{diag}(1, 1, \ldots, 1)$. The calculation of the dynamic susceptibilities can then be carried out by any standard numerical algorithm solving the linear system (5.7).

In order to complete the theoretical description we must return to the original magnetic moments $\boldsymbol{M}_\ell$. Inserting the linearized field (5.3) in equation (2.15) the corresponding linear approximation of the local moments reads

$$M_\ell^x \approx Q_\ell^x - \mathfrak{h}_\perp Q_\ell^y u_\ell \qquad M_\ell^y \approx Q_\ell^y + \mathfrak{h}_\perp Q_\ell^x u_\ell \qquad M_\ell^z \approx \rho\mathfrak{h}_\perp \ddot{u}_\ell \tag{5.8}$$

where u_ℓ is the terminal state (5.6). Hence the total moments are given by

$$\begin{aligned} \mu_1(\tau) &= \mu_1 + \Lambda\mathfrak{h}_\perp[\chi'_{12}\cos(\omega\tau) + \chi''_{12}\sin(\omega\tau)] \\ \mu_2(\tau) &= \mu_2 + \Lambda\mathfrak{h}_\perp[\chi'_{22}\cos(\omega\tau) + \chi''_{22}\sin(\omega\tau)] \\ \mu_3(\tau) &= \mu_3 + \Lambda\mathfrak{h}_\perp[\chi'_{32}\cos(\omega\tau) + \chi''_{32}\sin(\omega\tau)] \end{aligned} \tag{5.9}$$

where μ_1, μ_2, and μ_3 in the right-hand side are the static total moments of equation (4.3) and

$$\begin{aligned} \chi'_{12} &= -\frac{1}{\Lambda}\sum_\ell Q_\ell^y A_\ell \qquad & \chi''_{12} &= -\frac{1}{\Lambda}\sum_\ell Q_\ell^y B_\ell \\ \chi'_{22} &= \frac{1}{\Lambda}\sum_\ell Q_\ell^x A_\ell \qquad & \chi''_{22} &= \frac{1}{\Lambda}\sum_\ell Q_\ell^x B_\ell \\ \chi'_{32} &= \frac{\rho\omega}{\Lambda}\sum_\ell B_\ell \qquad & \chi''_{32} &= -\frac{\rho\omega}{\Lambda}\sum_\ell A_\ell \end{aligned} \tag{5.10}$$

are the sought-after total dynamic susceptibilities expressed in terms of the local ones with A_ℓ and B_ℓ determined from the linear system (5.7).

Now χ'_{12} and χ''_{12} manifestly vanish in the Néel state ($Q_\ell^y = 0$) and are also found to practically vanish for bias fields greater than $\mathfrak{h}_2$. They do acquire small finite values within the SSF region $[\mathfrak{h}_1, \mathfrak{h}_2]$ which are more a nuisance than a clear signature for the SSF transition. Similarly the sums in χ'_{32} and χ''_{32} are small and further suppressed by the factor $\rho\omega \ll 1$.

Therefore, although no additional effort is required to calculate all sums in equation (5.10), we shall confine our attention to the diagonal susceptibilities relabelled as

$$\chi'_{22} \equiv \chi' = \chi'(\omega, \mathfrak{h}) \qquad \chi''_{22} \equiv \chi'' = \chi''(\omega, \mathfrak{h}) \tag{5.11}$$

and examined in the following as functions of frequency ω and bias field $\mathfrak{h}$; for lattice size $\Lambda = 20$, easy-axis anisotropy $\delta = 1/4$, and dissipation constant $\lambda = 0.1$.

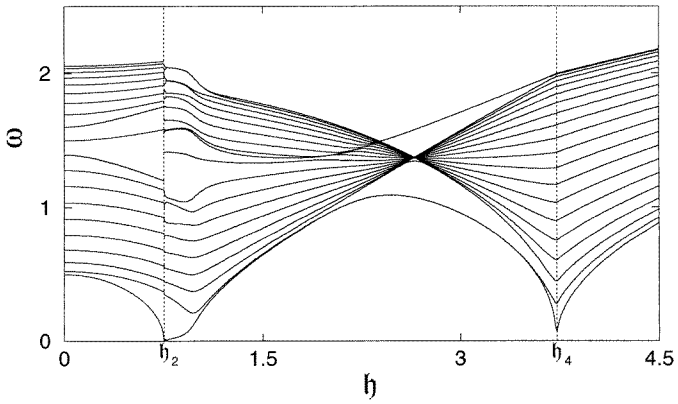

Figure 4. The magnon spectrum for $\Lambda = 20$ along the most likely ascending-field sequence reaching beyond ferromagnetic saturation.

Inspection of the linear system (5.7) suggests that potential resonances occur at frequencies such that

$$\det D = \det(C - \omega^2 I) = 0 \tag{5.12}$$

whose eigenvalues are determined numerically using as input the ground-state configuration $\boldsymbol{Q}_\ell$ calculated in section 4 at any given bias field $\mathfrak{h}$. We are thus in a position to complete the discussion of section 3 and calculate the normal frequencies $\omega = \omega(\mathfrak{h})$ for all $\mathfrak{h}$. Consider first the most likely ascending-field sequence in which the Néel state survives as a metastable local minimum beyond the true critical field $\mathfrak{h}_c = 0.682$, until the bias field crosses the value $\mathfrak{h}_2 = 0.75$ where a sudden SSF transition occurs. The corresponding eigenvalues of equation (5.12) are shown in figure 4 for a wide field range reaching beyond the critical field $\mathfrak{h}_4 = 3.73$ required for ferromagnetic saturation.

The overall appearance of figure 4 is similar to that of figure 7 in [12] in spite of the use of truncated dynamics. The main difference is that we now assume that the Néel state is trapped in its metastable phase in the region $[\mathfrak{h}_c, \mathfrak{h}_2]$. As a result the spectrum for the complete interval $[0, \mathfrak{h}_2]$ is the spectrum of the Néel state provisionally discussed in section 3 and shown schematically in figure 1. As expected the first and the eleventh modes counting from the bottom of figure 4 were found equal to the gap modes ω_1 and ω_2 of equations (3.5) and (3.6) which are valid for all Λ including $\Lambda = 20$. In particular, the lowest mode was numerically found to vanish at the critical field $\mathfrak{h}_2$ given analytically by equation (3.8). One should add that several important features of the calculated spectrum were already present in the earlier calculation of Nörtemann *et al* [23, 24].

The discontinuity of the spectrum at $\mathfrak{h}_2$ is yet another consequence of the first-order nature of the SSF transition. The imprint of the BSF transition is also made apparent in figure 4 by the observed crossover behaviour at $\mathfrak{h} \sim 1$. The evolution of the spectrum for larger field values is quite spectacular. Most eigenvalues cluster around a single value at the characteristic field

$\mathfrak{h}_{ch} \approx 2.65$ predicted for a cyclic chain by equation (3.12) and mildly corrected to account for the open chain considered here. However, a definite difference from the cyclic chain emerges with the appearance of surface modes whose eigenvalues are clearly separated below *and* above the continuum for fields in the region $\mathfrak{h} \sim \mathfrak{h}_{ch}$. Indeed the lowest gap mode (ω_1) in the Néel state is gradually joined by the next mode to evolve into a pair of nearly degenerate surface states with frequencies well within the lowest gap. Similarly the middle gap mode (ω_2) in the Néel state is joined by a nearby partner and they both work their way through the upper continuum to reappear as surface states with nearly degenerate frequencies above the continuum. A fifth gap mode can also be discerned just below the accumulation point of the eigenvalues at $\mathfrak{h} \sim \mathfrak{h}_{ch}$. Finally, the spectrum regroups itself into a more or less rigid continuum above the ferromagnetic transition which takes place at $\mathfrak{h}_4 = 3.73$.

A detailed analysis of the various surface states is certainly possible by examining the wavefunctions associated with the eigenvalue problem (5.12). Here we are mainly interested in their potential contributions to resonances in the dynamic susceptibilities χ' and χ''. The simple $q = 0$ rule known to apply for cyclic or infinite chains should be viewed with caution in the presence of open boundaries. Our numerical calculation is not based on any assumptions of that nature. Hence in figure 5 we illustrate the calculated frequency dependence of the dynamic susceptibilities for a number of typical values of the bias field $\mathfrak{h}$ taken along the described ascending-field sequence.

At low values of the bias field the main absorption peak occurs at the highest eigenfrequency which is accurately predicted by the numerical results of figure 4 or approximately by the bulk magnon spectrum (3.4) as

$$\omega_+^2(q = 0) = 2 + \delta + \sqrt{4 + \mathfrak{h}^2} \tag{5.13}$$

to within a minor finite-size correction. The above frequency accounts for the main resonance observed in figure 5 both at $\mathfrak{h} = 0$ and $\mathfrak{h} = 0.5$. A new low-frequency feature begins to emerge in the latter case due to absorption by the lowest gap mode with frequency ω_1 given analytically by equation (3.5). The contribution of this surface mode becomes increasingly significant when the Néel state enters its metastable phase for fields greater than $\mathfrak{h}_c = 0.682$, as illustrated in the $\mathfrak{h} = 0.735$ entry of figure 5 which exhibits a rather strong low-frequency signal.

When the bias field crosses the critical value $\mathfrak{h}_2 = 0.75$ of equation (3.8) the SSF transition becomes inevitable. Accordingly the low-frequency peak in the dynamic susceptibilities is suddenly quenched and is difficult to discern on the scale of the $\mathfrak{h} = 0.75$ entry of figure 5. Nevertheless, low-frequency absorption is again amplified, albeit to a lesser extent, when the field approaches the BSF crossover regime; as shown in the $\mathfrak{h} = 1$ entry of figure 5.

The superlattice is set on a clearly new course for fields beyond the BSF regime. Thus the low-frequency peak drifts to a higher frequency initially along the lowest eigenvalue of figure 4. However, it eventually shifts to the lower side of the continuum, i.e., to the third mode counting from the bottom of figure 4, as the bias field approaches the characteristic value $\mathfrak{h}_{ch} \approx 2.65$ of equation (3.12). Meanwhile the highest eigenfrequency loses its intensity and is replaced by a secondary peak drifting along with the middle gap mode on its way to emerging as a surface state above the continuum. For $\mathfrak{h} > \mathfrak{h}_{ch}$ a partial reversal takes place and the two peaks observed at, say, $\mathfrak{h} = 3$ correspond to the frequencies of the upper side of the continuum and of the highest surface mode. Finally, above the ferromagnetic transition, e.g., at $\mathfrak{h} = 4$, the two peaks merge into a single clear signal at the highest magnon frequency given by equation (3.14) as

$$\omega^2(k = 0) = \delta + \mathfrak{h} \tag{5.14}$$

again to within a minor finite-size correction.

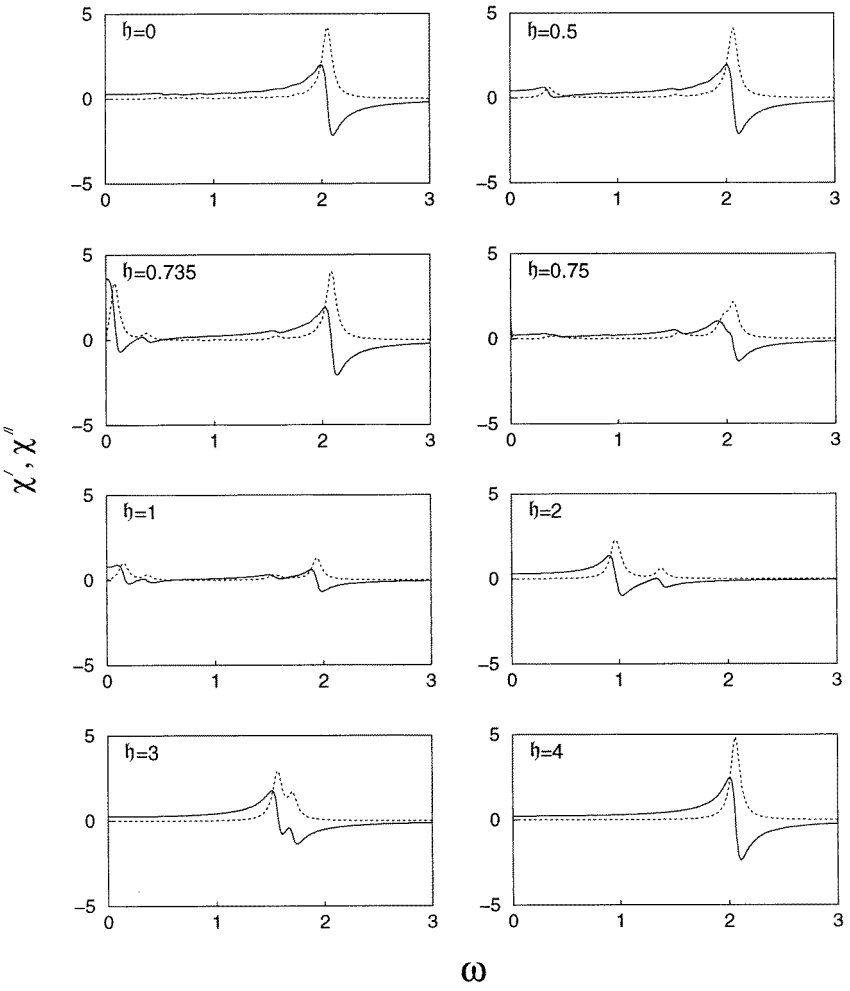

Figure 5. Dynamic susceptibility as a function of frequency for representative values of the bias field along the most likely ascending-field sequence. The real part (χ') is depicted by a solid line and the imaginary part (χ'') by a dotted line.

Therefore an experiment that would determine the frequency dependence of the susceptibilities would probe in detail the dynamics of the superlattice. However, to the best of our knowledge, such an experiment has not yet been performed. Instead the susceptibilities were measured as functions of the DC bias field with an AC field also pointing along the easy axis and operating at a fixed very low frequency [14]. Here and in the calculation of the above reference the AC field is assumed to be perpendicular to the easy axis. In the upper panel of figure 6 we display the field dependence of the dynamic susceptibilities calculated here at the fixed relatively low frequency $\omega = 0.1$. This result is consistent in its gross features with the calculation in [14].

The strong signal just below $\mathfrak{h}_2 = 0.75$ as well as the lower bump near the BSF regime $\mathfrak{h} \sim 1$ are consistent with the frequency dependences of figure 5. The first peak is expected and numerically verified to become increasingly sharp at lower frequencies and its location

approaches the critical field $\mathfrak{h}_2$ from below. It is then clear that the most likely ascending-field sequence yields a sensitive probe of the critical field where the Mills–Saslow surface magnon mode turns soft [2], but bypasses the finer details of the SSF transition. On the other hand, these important details could be accessible through hysteresis.

Hence we recall the discussion of section 4 and consider the calculation of dynamic susceptibilities along the 'true' hysteresis curve given by the dotted line of figure 2. The corresponding normal frequencies calculated from equation (5.12) are shown in figure 7 and differ from those of figure 4 only in the field interval $[\mathfrak{h}_1, \mathfrak{h}_2]$. The frequency dependence of the diagonal susceptibilities $\chi' = \chi'_{22}$ and $\chi'' = \chi''_{22}$ is depicted in figure 8 for two typical field values $\mathfrak{h} = 0.675$ and $\mathfrak{h} = 0.725$ within the region of metastability ($\mathfrak{h} < \mathfrak{h}_c$) and absolute

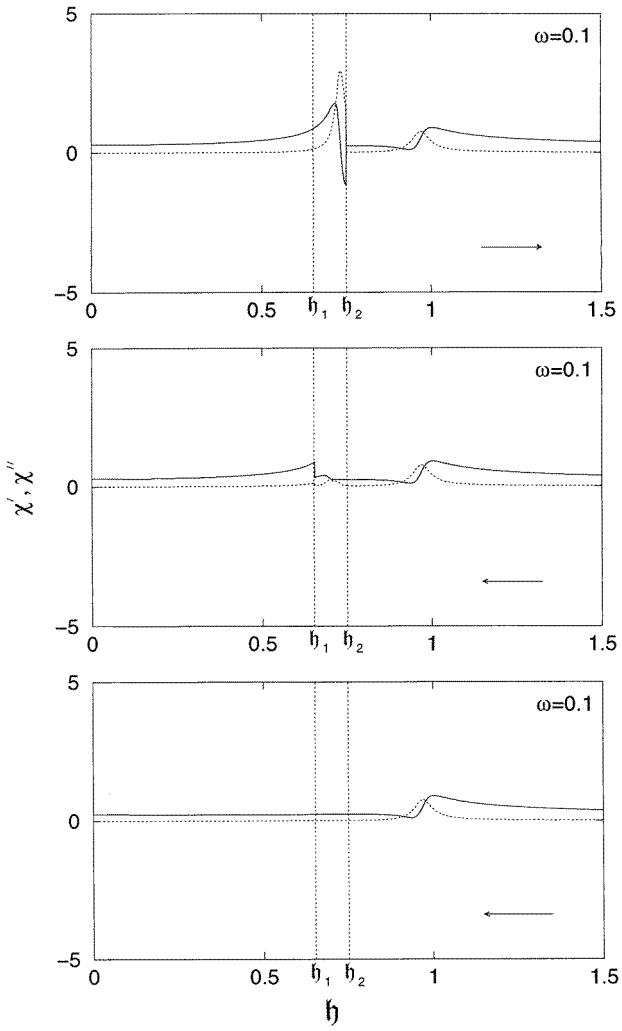

Figure 6. Field dependence of the dynamic susceptibility at a fixed low frequency $\omega = 0.1$. The arrow in each frame indicates the direction of increasing (decreasing) bias field along the three field sequences as described in the text.

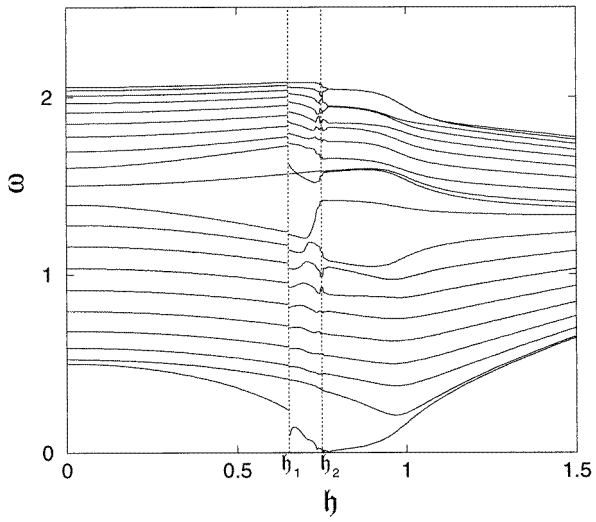

Figure 7. The magnon spectrum of figure 4 with the exception of the field interval $[\mathfrak{h}_1, \mathfrak{h}_2]$ where the spectrum is now calculated in the SSF instead of the Néel state.

stability ($\mathfrak{h} > \mathfrak{h}_c$) of the true SSF state, respectively. In both cases the low-frequency features are tamed. As a result the field dependence along the descending sequence illustrated in the middle panel of figure 6 shows no dramatic variations in the SSF region $[\mathfrak{h}_1, \mathfrak{h}_2]$. One should further recall our earlier comment that the off-diagonal susceptibilities χ'_{12} and χ''_{12} also acquire finite values of comparable variation in the same field region. The overall conclusion is that a clear signal for the finer details of the SSF transition does not seem feasible through dynamic response in a transverse AC magnetic field.

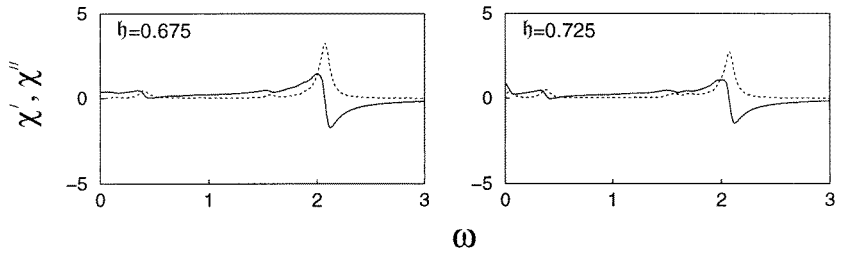

Figure 8. Dynamic susceptibility as a function of frequency for two typical values of the bias field in the regions of metastability ($\mathfrak{h} = 0.675$) and absolute stability ($\mathfrak{h} = 0.725$) of the SSF state.

Furthermore, the descending-field sequence assumed in the middle panel of figure 6 is artificial in an important respect. The corresponding hysteresis curve is realized only if the nominal field $\mathfrak{h}_0$ at which the cycle is reversed is chosen to be just above the critical field $\mathfrak{h}_2 = 0.75$. When $\mathfrak{h}_0$ is sufficiently large the superlattice loses memory of the SSF transition and is locked into a symmetric state. Thus the generic hysteresis curve shown by open circles in figure 2 extends all the way down to vanishing field, reflecting the fact that a domain wall is trapped in a metastable state near the centre of the superlattice. The field dependence of the susceptibilities along the generic hysteresis curve is depicted in the lower panel of figure 6 and continues to display the standard BSF peak at $\mathfrak{h} \sim 1$ but is featureless in the SSF region

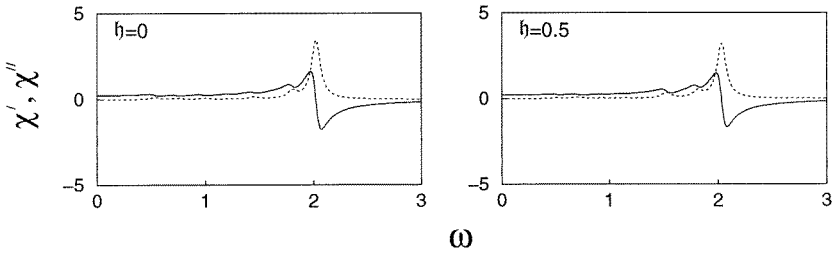

Figure 9. Dynamic susceptibility as a function of frequency in the presence of a bulk domain wall trapped at the centre of the chain for two typical values of the bias field.

$[\mathfrak{h}_1, \mathfrak{h}_2]$. This result is a consequence of the absence of an interesting low-frequency behaviour in the dynamic susceptibilities, a fact illustrated in figure 9 for the two representative field values $\mathfrak{h} = 0$ and $\mathfrak{h} = 0.5$. Therefore lack of structure in the dynamic susceptibilities near the SSF region would provide indirect experimental evidence for the realization of the elongated hysteresis curve of figure 2.

We have additionally examined the spectrum of normal frequencies in the presence of a bulk domain wall at the centre of a finite chain. This spectrum exhibits a nearly zero-frequency bulk mode, instead of a surface gap mode, which is a finite-lattice analogue of the strict zero mode that would occur in the continuum limit ($\delta \to 0$) of an infinite lattice ($\Lambda \to \infty$) reflecting translation invariance. It is thus not surprising that such a mode is not excited by the uniform AC field and is not conspicuous in figure 9.

The preceding analysis may be carried further to address the question of local stability of a bulk domain wall trapped at the centre of a finite chain. In fact, at vanishing bias field, the lowest squared normal frequency was found to be negative ($\omega^2 \sim -10^{-4}$) for $\Lambda = 20$ and positive ($\omega^2 \sim 10^{-5}$) for $\Lambda = 100$. Therefore the domain wall is actually a marginally unstable saddle point on a sufficiently short chain. More generally one should expect that a bulk domain wall would become locally stable on a chain that exceeds a certain critical size $\Lambda = \Lambda_c(\delta, \mathfrak{h})$ which is a function of anisotropy δ and bias field $\mathfrak{h}$. As a consequence the elongated hysteresis curve shown by open circles in figure 2 should become more robust on larger superlattices.

The numerical method followed in the present work is completely elementary and easy to implement. Nevertheless, an interesting alternative was suggested by the authors of [14]. Within the context of the truncated dynamics the method of the above reference would amount to solving the initial-value problem for the *nonlinear* dissipative sine–Gordon equation (5.2) in the presence of a weak AC field. The dynamic susceptibilities would then be extracted from the steady state acquired by $\phi_\ell(\tau)$ when the DC bias field is changed adiabatically. We have actually implemented the method for equation (5.2) and reproduced some of the described results for special values of the parameters. Our preference to the standard linear response theory adopted in the text was due to its ability to provide detailed information on the normal frequencies of the system. However, the method of [14] is more natural and will certainly play an important role in future micromagnetic calculations.

6. Concluding remarks

Although the main features of the SSF transition are clearly understood, a number of more detailed issues remain to be investigated both theoretically and experimentally. The nature

of the hysteresis is probably the most urgent issue that has not been completely settled. Furthermore, the finer details of the transition have not yet been resolved and could, in fact, be irrelevant to actual experiments.

One should thus address and possibly quantify the question of robustness in the presence of disorder and/or noise. Static disorder may result from a variation of the parameters as one moves from one layer to the next. Similarly noise may be induced dynamically either by the external field or by internal fluctuations including a partial lack of coherence in the moment of each layer. A formulation of the relevant stochastic dynamics might prove fruitful especially near the SSF transition where the effective potential displays a multitude of local minima with energies that differ only slightly. In particular, one might be able to explain in detail a certain loss of memory and irreversibility that are responsible for the elongated hysteresis curve of figure 2.

Throughout this paper we have confined our attention to an even superlattice. The main difference in the Néel state of an odd superlattice is that the moments of the two outer layers point in the same direction. Therefore when the bias field is applied along the direction of the outer moments a SSF transition is absent and the system proceeds directly to the BSF transition. When the field is applied in the opposite direction a SSF transition takes place at both ends. Thus the picture appears to be more complicated on an odd superlattice but does not add anything fundamentally new. In any case, all calculations can be repeated for an odd chain without difficulty.

Acknowledgments

I am grateful to D L Mills for encouragement, and to A Orendacova and M Orendac for providing me with some useful references. The work was supported in part by a grant from the EEC (CHRX-CT93-0332).

Appendix. Dynamics of a single moment

We return to the discussion of section 2 and consider the special limit of vanishing exchange constant ($J = 0$) in which the moments of the various layers decouple. The dynamics of each moment $\boldsymbol{M} = (M_x, M_y, M_z) = (\sin\theta\cos\phi, \sin\theta\sin\phi, \cos\theta)$ is then governed by the Hamiltonian

$$W = \frac{1}{2}(D\sin^2\theta\sin^2\phi + D_0\cos^2\theta) - H\sin\theta\cos\phi - H_\perp\cos(\Omega t)\sin\theta\sin\phi \tag{A1}$$

where the external field consists of a DC component of strength H along the easy, x-axis and an AC component of amplitude $H_\perp$ and frequency Ω along the y-axis. For the moment we make no assumptions on the relative strength of the anisotropy constant D_0.

The corresponding Landau–Lifshitz equations read

$$\begin{aligned}\sin\theta\frac{\partial\phi}{\partial t} + \gamma\frac{\partial\theta}{\partial t} &= (D_0 - D\sin^2\phi)\cos\theta\sin\theta + [H\cos\phi + H_\perp\cos(\Omega t)\sin\phi]\cos\theta \\ \frac{\partial\theta}{\partial t} - \gamma\sin\theta\frac{\partial\phi}{\partial t} &= D\sin\theta\cos\phi\sin\phi + H\sin\phi - H_\perp\cos(\Omega t)\cos\phi\end{aligned} \tag{A2}$$

and our task is to determine the evolution of the moment induced by a weak AC field. One may then invoke the linear approximation $\theta \approx \pi/2 - gH_\perp$ and $\phi \approx fH_\perp$ or

$$M_x \approx 1 - \frac{1}{2}(f^2 + g^2)H_\perp^2 \qquad M_y \approx fH_\perp \qquad M_z \approx gH_\perp \tag{A3}$$

where the amplitudes f and g satisfy the linear system

$$\begin{aligned} &\frac{\partial f}{\partial t} - \gamma \frac{\partial g}{\partial t} - \Omega_2 g = 0 \qquad && \frac{\partial g}{\partial t} + \gamma \frac{\partial f}{\partial t} + \Omega_1 f = \cos(\Omega t) \\ &\Omega_1 \equiv D + H && \Omega_2 \equiv D_0 + H. \end{aligned} \tag{A4}$$

At large times, transients damp out exponentially and the terminal state is described by the particular solution

$$f = A\cos(\Omega t) + B\sin(\Omega t) \qquad g = \Gamma\cos(\Omega t) + \Delta\sin(\Omega t) \tag{A5}$$

where the dynamic susceptibilities are given by

$$\begin{aligned} A &= \frac{\Omega_2(\Omega_1\Omega_2 - \Omega^2) + \gamma^2\Omega_1\Omega^2}{[\Omega_1\Omega_2 - (1+\gamma^2)\Omega^2]^2 + \gamma^2(\Omega_1+\Omega_2)^2\Omega^2} \\ B &= \frac{\gamma\Omega[\Omega_2^2 + (1+\gamma^2)\Omega^2]}{[\Omega_1\Omega_2 - (1+\gamma^2)\Omega^2]^2 + \gamma^2(\Omega_1+\Omega_2)^2\Omega^2} \\ \Gamma &= \frac{\gamma(\Omega_1+\Omega_2)\Omega^2}{[\Omega_1\Omega_2 - (1+\gamma^2)\Omega^2]^2 + \gamma^2(\Omega_1+\Omega_2)^2\Omega^2} \\ \Delta &= \frac{\Omega[(1+\gamma^2)\Omega^2 - \Omega_1\Omega_2]}{[\Omega_1\Omega_2 - (1+\gamma^2)\Omega^2]^2 + \gamma^2(\Omega_1+\Omega_2)^2\Omega^2}. \end{aligned} \tag{A6}$$

For small values of the dissipation constant ($\gamma \ll 1$) resonance occurs at the characteristic frequency $\Omega = \sqrt{\Omega_1\Omega_2}$.

Thus the component of the moment along the easy axis undergoes a negligible second-order modulation around its ground-state value, $M_x = 1$, whereas the projection of the moment on the yz-plane is elliptically polarized. The length of the ellipse axes and their relative orientation in the yz-plane are sensitive functions of frequency Ω and bias field H especially near resonance. However, the picture simplifies substantially when D_0 is much larger than all other scales involved. This limit may be studied either by starting from the exact susceptibilities (A6) or by first implementing the truncated dynamics of section 2; as is done in the remainder of this appendix.

Since an exchange constant is no longer present the rescaled variables of equations (2.9) and (2.10) are redefined as

$$\begin{aligned} &\rho = \sqrt{D/D_0} \qquad && \Omega_0 = \sqrt{DD_0} \qquad && \tau = \Omega_0 t \\ &\lambda = \gamma/\rho && \mathfrak{h} = H/D && \mathfrak{h}_\perp = H_\perp/D \end{aligned} \tag{A7}$$

and we again introduce a field χ via $\theta = \pi/2 - \rho\chi$. In the limit of small ρ, the truncated dynamics is governed by

$$\chi = \dot{\phi} \qquad \ddot{\phi} + \lambda\dot{\phi} + \cos\phi\sin\phi + \mathfrak{h}\sin\phi = \mathfrak{h}_\perp\cos(\omega\tau)\cos\phi \tag{A8}$$

where the dot stands for differentiation with respect to τ and $\omega = \Omega/\Omega_0$ is the normalized frequency. Accordingly the approximate moment is given by equation (2.15) restricted to a single site.

Dynamic response is now based on the truncated equation (A8) which is solved to leading order in $\mathfrak{h}_\perp$ by $\phi \approx u\mathfrak{h}_\perp$ where u satisfies the linear equation

$$\ddot{u} + \lambda\dot{u} + (1+\mathfrak{h})u = \cos(\omega\tau) \tag{A9}$$

whose relevant particular solution is

$$\begin{aligned} &u = \alpha\cos(\omega\tau) + \beta\sin(\omega\tau) \\ &\alpha = \frac{1+\mathfrak{h}-\omega^2}{(1+\mathfrak{h}-\omega^2)^2 + \lambda^2\omega^2} \qquad \beta = \frac{\lambda\omega}{(1+\mathfrak{h}-\omega^2)^2 + \lambda^2\omega^2}. \end{aligned} \tag{A10}$$

The projection of the moment on the yz-plane is then given by

$$\begin{aligned} M_y &\approx u\mathfrak{h}_\perp = [\alpha\cos(\omega\tau) + \beta\sin(\omega\tau)]\mathfrak{h}_\perp \\ M_z &\approx \rho\dot{u}\mathfrak{h}_\perp = \rho\omega[\beta\cos(\omega\tau) - \alpha\sin(\omega\tau)]\mathfrak{h}_\perp \end{aligned} \tag{A11}$$

and describes an ellipse whose major axis is now fixed along the y-direction, and the minor axis is relatively depressed. Hence the picture derived is consistent with the intuitive expectation that out-of-plane fluctuations are small at large D_0. Furthermore, if we introduce the rescaled variables (A7) in the exact susceptibilities (A6) and then take the limit of large D_0, the truncated result (A10) is reproduced. We have also plotted the exact and the truncated susceptibilities and found them to be graphically indistinguishable when $D_0/D = 100$. The agreement continues to be satisfactory at $D_0/D = 10$ and strongly influenced our decision to adopt the truncated dynamics.

References

[1] Mills D L 1968 *Phys. Rev. Lett.* **20** 18
[2] Mills D L and Saslow W 1968 *Phys. Rev.* **171** 488
[3] Keffer F and Chow H 1973 *Phys. Rev. Lett.* **31** 1061
[4] Baibich M N, Broto J M, Fert A, Nguyen Van Dau F, Petroff F, Eitenne P, Greuzet G, Friederich A and Chazeles J 1988 *Phys. Rev. Lett.* **61** 2472
[5] Fullerton E E, Conover M J, Mattson J E, Sowers C H and Bader S D 1993 *Phys. Rev.* B **48** 15 755
[6] Wang R W, Mills D L, Fullerton E E, Mattson J E and Bader S D 1994 *Phys. Rev. Lett.* **72** 920
[7] Trallori L, Politi P, Rettori A, Pini M G and Villain J 1994 *Phys. Rev. Lett.* **72** 1925
[8] Trallori L, Politi P, Rettori A, Pini M G and Villain J 1995 *J. Phys.: Condens. Matter* **7** L451
[9] Micheletti C, Griffiths R B and Yeomans J M 1997 *J. Phys. A: Math. Gen.* **30** L233
[10] Papanicolaou N 1998 *J. Phys.: Condens. Matter* **10** L131
[11] Papanicolaou N 1995 *Phys. Rev.* B **51** 15 062
[12] Wang R W and Mills D L 1994 *Phys. Rev.* B **50** 3931
[13] Wang R W, Mills D L, Fullerton E E, Kumar S and Grimsditch M 1996 *Phys. Rev.* B **53** 2627
[14] Rakhmanova S, Mills D L and Fullerton E E 1998 *Phys. Rev.* B **57** 476
[15] Landau L and Lifshitz E 1935 *Phys. Z. Sowjetunion* **8** 153
[16] Gilbert T L 1955 *Phys. Rev.* **100** 1243
[17] Kikuchi R 1956 *J. Appl. Phys.* **27** 1352
[18] Stamps R L, Camley R E, Nörtemann F C and Tilley D R 1993 *Phys. Rev.* B **48** 15 740
[19] Mikeska H J 1978 *J. Phys. C: Solid State Phys.* **11** L29
[20] Mikeska H J 1980 *J. Phys. C: Solid State Phys.* **13** 2913
[21] Leung K M, Hone D W, Mills D L, Riseborough P S and Trullinger S E 1980 *Phys. Rev.* B **21** 4017
[22] Lemmens L F, Kimura I and de Jonge W J M 1986 *J. Phys. C: Solid State Phys.* **19** 139
[23] Nörtemann F C, Stamps R L, Carrico A S and Camley R E 1992 *Phys. Rev.* B **46** 10 847
[24] Nörtemann F C, Stamps R L and Camley R E 1993 *Phys. Rev.* B **47** 11 910